

Oxygen Vacancy Promoting Catalytic Dehydration of Formic Acid on TiO₂(110) by in Situ Scanning Tunneling Microscopic Observation

Masaki Aizawa,[†] Yoshitada Morikawa,[§] Yoshimichi Namai,[†] Harumo Morikawa,[†] and Yasuhiro Iwasawa^{*,†}

Department of Chemistry, Graduate School of Science, The University of Tokyo, Hongo, Bunkyo-ku, Tokyo 113-0033, Japan, and The Institute of Scientific and Industrial Research, Osaka University, 8-1 Mihogaoka, Ibaraki, Osaka 567-0047, Japan

Received: May 8, 2005; In Final Form: August 8, 2005

The catalytic dehydration reaction processes of formic acid on a TiO₂(110) surface at 350 K have been studied to visualize reaction intermediates and their dynamic behaviors by scanning tunneling microscopy. Three types of configurations of adsorbed formates on the surface were identified by their shapes and positions in STM images. Successive STM observations revealed transformations among the three configurations, i.e., bridge formate on a 5-fold coordinated Ti⁴⁺ row, bridge formate on an oxygen vacancy site with an oxygen atom of formate and on a 5-fold coordinated Ti⁴⁺ ion and with the other formate oxygen atom, and a monodentate formate on an oxygen vacancy site with an oxygen atom of formate. The decomposition of the monodentate formate to carbon monoxide and hydroxyl was also imaged, which is a rate-determining step in the catalytic dehydration of formic acid. Combined with first-principle DFT calculations, the overall reaction processes of the catalytic dehydration of formic acid on the surface have been elucidated. Oxygen vacancies on the surface that can be produced by dehydration of two hydroxyls in situ under the catalytic reaction conditions are essential for the reaction.

Introduction

Transition metal oxides with characteristic acid–base and redox properties, which are different from those of metals and one-component semiconductors, have attracted considerable interest from both fundamental and technological points of view due to a wide range of the applications to heterogeneous catalysis,^{1–5} solar cells,⁶ photocatalysis,^{7,8} biocompatible implants,⁹ and so on.¹⁰ A key issue in developing catalytic materials and systems is understanding the site-specific surface dynamic processes of adsorbed molecules and reaction intermediates on an atomic scale to find atom-resolved structure–activity relationships. However, few reaction mechanisms for heterogeneous catalysis on an atomic scale are elucidated to date, though many modern sophisticated techniques for surface characterization have been developed. Atom-resolved scanning probe microscopies, such as scanning tunneling microscopy (STM) and noncontact atomic force microscopy (NC-AFM), have allowed us to visualize individual atoms and molecules at surfaces, and to determine the reaction sites.^{11–16}

TiO₂ is one of the most well-studied metal oxides.^{10,17,18} It is used in heterogeneous catalysis, photo catalysis, solar cells, gas sensors, and white pigment, and as a gate insulator for the next generation of metal-oxide-semiconductor field-effect transistors. Despite the importance of TiO₂ in such applications, particularly catalysis, atomic/molecular-scale understanding of catalytic reactions on the surface still remains a subject to be tackled.

The adsorption and decomposition of formic acid (HCOOH) on rutile TiO₂(110) has been intensively studied as a prototypical system of catalytic reactions.^{19–48} Formic acid decomposes on a TiO₂(110) surface in two ways, dehydratively and dehydro-

genatively. The two types of the reactions are switched over depending on the reaction temperature and the gas-phase pressure.^{11,26,29,33,43} In both dehydration and dehydrogenation reactions, an adsorbed formate anion (HCOO[−]) is an important intermediate. Previous STM studies^{27,28,30–32,36,41} imaged individual formate species on two 5-fold coordinated Ti⁴⁺ ions in a bridge configuration and their migration on the Ti⁴⁺ rows. Although the diffusion of formate ions occurred because of the repulsive force between adsorbates, no chemical reaction on the surface was monitored by STM.

On the other hand, the existence of another type of configuration for formates on TiO₂(110) on highly defective surfaces or under a high exposure of formic acid has also been demonstrated by STM,⁴⁴ infrared reflection absorption spectroscopy (IRAS),⁴⁰ electron energy loss spectroscopy (EELS),⁴⁶ and near edge X-ray absorption fine structure (NEXAFS).⁴⁷ In this configuration, a formate species occupies an oxygen vacancy with an oxygen atom from the formate, and occupies a 5-fold coordinated Ti⁴⁺ ion with the other oxygen atom. Many studies^{37,40,44–49} on the relation between formic acid decomposition and oxygen vacancy have been performed to explore the origin of the catalytic property of metal oxides. On a highly defective TiO₂(110) surface prepared in a controlled manner, the CO selectivity in formic acid decomposition increases and the amount of produced H₂O relative to the CO amount decreases, indicating a correlation between oxygen vacancies and the dehydration reaction of formic acid,⁴⁵ whereas the selectivities for the formations of CO, H₂O, CO₂, and H₂ do not significantly change on Ar⁺-ion-bombarded TiO₂(110) surfaces.⁴⁹

Recently, we have examined the dehydration processes of formic acid on rutile TiO₂(110) by first-principle density functional theoretical (DFT) calculations, and found that a simple decomposition process of bridge formates on the stoichiometric surface is energetically unfavorable.⁴⁸ Instead, a

* Tel: +81-3-5841-4363. Fax: +81-3-5800-6892. E-mail: iwasawa@chem.s.u-tokyo.ac.jp.

[†] The University of Tokyo.

[§] Osaka University.

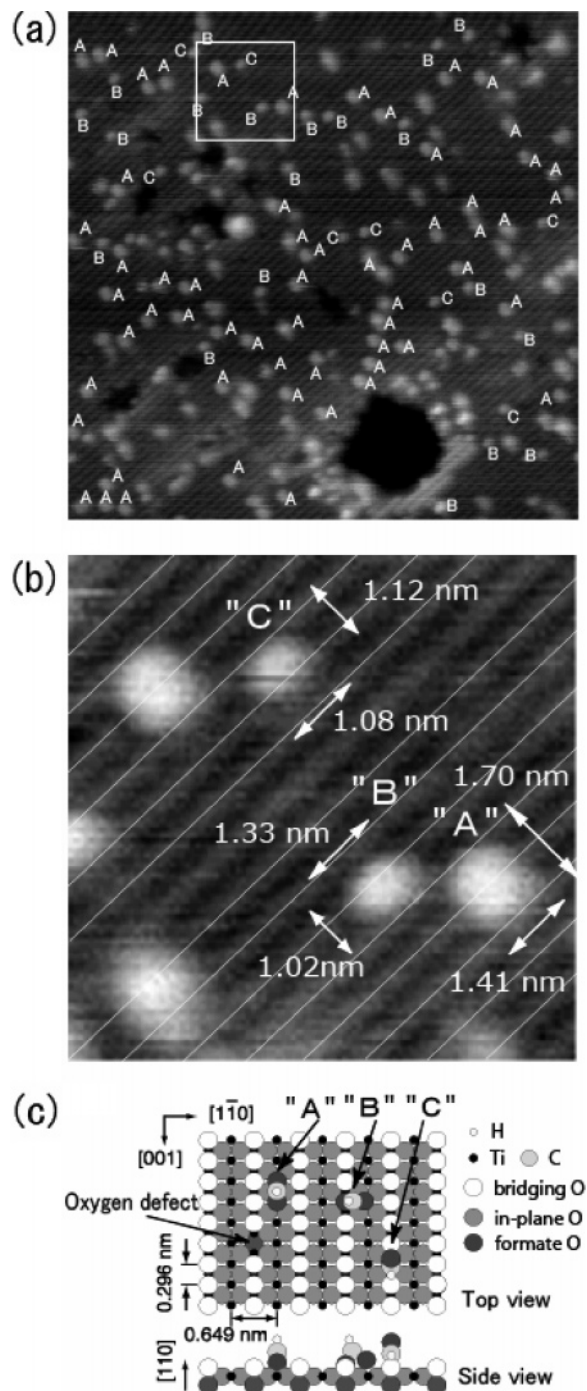


Figure 1. (a) STM image (CCT, $40 \times 40 \text{ nm}^2$, $V_s = 1.2 \text{ V}$, $I_t = 0.1 \text{ nA}$) of $\text{TiO}_2(110)$ exposed to 1 L of formic acid at room temperature, followed by annealing at 350 K for 400 min. Three types of formate species labeled as A, B, and C are observed. (b) The white square area in (a) is enlarged. The sizes of contrasts for each formate along the [001] and [110] directions are indicated. (c) Schematic models of the three formate configurations.

decomposition process via monodentate formate adsorbed on an oxygen vacancy is more favorable, and the calculated activation barrier of this process is 129 kJ mol^{-1} , which is consistent with an experimental value of 120 kJ mol^{-1} . These results tempted us to image the behavior of reaction intermediate species at a reaction temperature by STM to elucidate elementary steps in the catalytic dehydration reaction of formic acid on a $\text{TiO}_2(110)$ surface.

In the present study, we have performed STM observations of the surface reactions of formates on $\text{TiO}_2(110)$ at reaction

temperatures, and have identified three configurations of formates, two of which are hard to observe at room temperature (RT). We have also observed dynamic processes from a formate configuration to another configuration involving the rate-determining step of the dehydration reaction. These STM observations, with aid of the first-principle DFT calculations, revealed the overall reaction paths of the catalytic decomposition of formic acid, in which oxygen vacancies behave as catalytic reaction sites.

Methods

2.1. Experimental Method. The experiments were performed in an ultrahigh vacuum STM (JEOL JSTM4500VT) equipped with an Ar^+ -ion gun, a quadrupole mass spectrometer, and AES-LEED optics. The base pressure was $2 \times 10^{-8} \text{ Pa}$. A polished $\text{TiO}_2(110)$ wafer of $6.5 \times 1 \times 0.25 \text{ mm}^3$ (Earth Chemical) was calcined at 1000 K in air and put into the STM chamber. The surface was cleaned with cycles of Ar^+ ion sputtering (3 keV for 3 min) and annealing at 900 K for 2 min under UHV. Constant current topographies (CCTs) were obtained at RT and at 350 K with electrochemically etched W tips. Deuterated formic acid (DCOOD , Aldrich, 98% purity) was purified by repeated freeze–pump–thaw cycles, and introduced into the chamber by backfilling. The surface temperature of the crystal was monitored by an infrared radiation thermometer.

2.2. Computational Method. All calculations were carried out using the program package STATE (Simulation Tool for Atom TEchnology), which has been successfully applied for molecular adsorption and reactions over semiconductor, metal, and metal oxide surfaces.^{48,50–54} We adopted a generalized gradient approximation (GGA) in the density functional theory (DFT),^{55,56} and the Perdew, Burke, and Ernzerhof formula⁵⁷ as the exchange-correlation energy functional. Pseudopotentials of H 1s, C 2p, O 2p, Ti 3p, and 3d states were constructed by Vanderbilt's scheme,⁵⁸ whereas other components were constructed by an optimized norm-conserving scheme by Troullier and Martins.⁵⁹ The cutoff energy for the wave function is 25 Ry, and that for the augmentation charge is 225 Ry. The lattice constants of rutile TiO_2 are optimized to be $a = 0.4665 \text{ nm}$ and $c/a = 0.642$, being in good agreement with the experimental values of $a = 0.4594 \text{ nm}$ and $c/a = 0.644$. We used a repeated slab model, and the number of O–Ti–O triple layers ($N_{\text{O–Ti–O}}$) is changed from 3 to 7 (see below). The vacuum region of more than 1 nm is inserted between two neighboring slabs. Adsorbates are introduced on only one side of each slab. The integration within the surface Brillouin zone was done using 2×4 uniform mesh of \mathbf{k} -points for a 1×1 unit cell, and similar mesh points were used for other surface unit cells. For the structural optimization, atoms of adsorbates and the two top O–Ti–O layers were allowed to relax, whereas the bottom O–Ti–O layer was fixed at its ideal bulk position. The structural optimization was continued until the maximum force became less than $50 \text{ kJ mol}^{-1} \text{ nm}^{-1}$. STM images were simulated by the Tersoff and Hamann scheme.⁶⁰ To simulate constant-current-mode STM images for empty states, we integrated the local density of states from the lowest unoccupied (LU) state to 1 eV above the LU state.

$$\rho^{\text{LDOS}}(\mathbf{r}; E) = \sum_{\mathbf{k}}^{\text{all states}} |\phi_{\mathbf{k}}(\mathbf{r})|^2 \delta(E - E_{\mathbf{k}})$$

$$\rho^{\text{empty}}(\mathbf{r}) = \int_{E_{\text{LU}}}^{E_{\text{LU}} + 1 \text{ eV}} \rho^{\text{LDOS}}(\mathbf{r}; E) dE$$

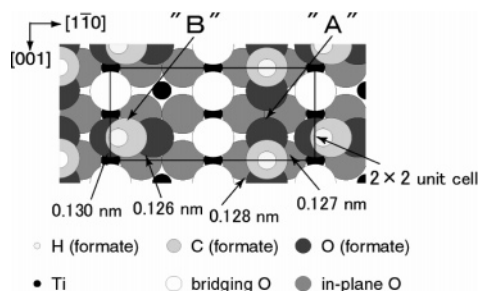


Figure 2. Unit cell (2×2) of a rutile $\text{TiO}_2(110)$ surface used to optimize the A and B configurations of the formate species. Formates in configurations A and B are on the left and right Ti rows in the unit cell, respectively. C–O bond lengths of the formates are indicated.

Then the height of the isodensity surface ($\rho^{\text{empty}}(\mathbf{r}) = 3.4 \times 10^{-2} \text{ e/nm}^3$) was traced, which corresponds to STM images in the constant-current mode.

Results and Discussion

3.1. STM Observation of Formates on $\text{TiO}_2(110)$ at Reaction Temperature. Figure 1a shows a typical STM image of a $\text{TiO}_2(110)$ surface exposed to 1 L ($1 \text{ L} = 1.33 \times 10^{-4} \text{ Pa s}$) of formic acid at RT followed by annealing at 350 K for 400 min. A clean $\text{TiO}_2(110)-(1 \times 1)$ surface is constituted by alternative rows of titanium and oxygen atoms at an interval of 0.649 nm. The STM image was recorded at a positive sample bias of +1.2 V, in which the titanium rows are observed as bright lines as shown in Figure 1a. Formic acid dissociatively adsorbs at RT to form formate anions as proved by UPS.²⁹ Formate anions are imaged as bright contrasts (Figure 1a). Very recently we reported three different formate species located in different sites of the surface in a preliminary STM study.⁴⁸ The present STM observation at 350 K (Figure 1a,b) confirms the existence of formates at three different locations: formate on a Ti row (configuration A), formate between a Ti row and an O row (configuration B), and formate on an O row (configuration C). Details of these three configurations were determined by DFT calculations.⁴⁸ A formate in the A configuration is a bridge formate on two 5-fold coordinated Ti^{4+} ions, and it is in the same configuration as that previously reported by STM observations at RT.^{27,30–33} A formate in the B configuration is a bridge formate on an oxygen vacancy site with an oxygen atom of formate and on a 5-fold coordinated Ti^{4+} ion with another oxygen atom of formate. A formate in the C configuration is a monodentate formate on an oxygen vacancy site with an oxygen atom of formate as shown in Figure 1c.

The O–C–O planes of species A and B are aligned along the [001] and [110] directions, respectively, according to a simple speculation about the formate molecular orbital. The STM image of Figure 1b reveals that the formate species in the bridge configurations A and B have ellipsoidal shapes. From the topographical height analysis, the major and minor axes of the species A ellipse are along the [110] direction with a size of 1.70 nm and along the [001] direction with a size of 1.41 nm, respectively, as indicated in Figure 1b. The major and minor axes of the species B ellipse are along the [001] direction with a size of 1.33 nm and along the [110] direction with a size of 1.02 nm, respectively. Because the present STM observation was performed in the positive-sample-bias condition, the ellipsoidal shapes of these species are due to the lowest unoccupied molecular orbital (LUMO) of the formates, which expands in the direction perpendicular to the O–C–O plane.²⁶ Thus, the O–C–O planes are along the minor axis of the ellipses: the [001] direction for A, and the [110] direction for

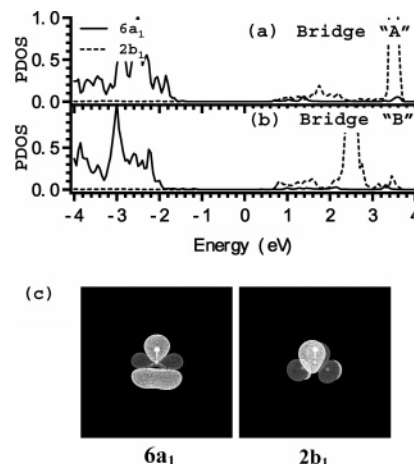


Figure 3. Projected density of states of the $6a_1$ and $2b_1$ states of formate in (a) the configuration A and (b) the configuration B. (c) Molecular orbitals of $6a_1$ and $2b_1$ states for isolated formate anion.

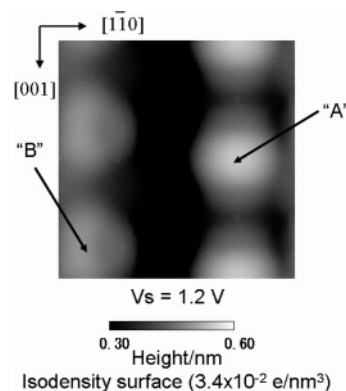


Figure 4. Calculated empty-state STM images of formates in the configurations A and B adsorbed on the 2×2 unit cell of the $\text{TiO}_2(110)$ surface. Sample-bias voltage is 1.2 V.

B. The STM images are correlated to the molecular orbitals in more detail by the first-principle DFT calculation in section 3.2.

Unlike the bridge configurations A and B, the monodentate formate species C is observed as a circular protrusion (1.12 nm along the [001] direction and 1.08 nm along the [110] direction) in Figure 1b. Although the O–C–O plane is illustrated along the [001] direction in Figure 1c, the species C in a monodentate configuration can rotate thermally around the Ti–O bond. The existing A:B:C formate ratio on the surface exposed to 1 L of formic acid followed by annealing at 350 K for 400 min was estimated to be 10:7:3 by 113 contrasts in several independent STM observations. The ratio approximately reflects the relative stability of the formates.

3.2 Structure and Density of States of Adsorbed Formates on $\text{TiO}_2(110)$. We have optimized the structures of the bridge configurations A and B of adsorbed formates in a $\text{TiO}_2(110)-(2 \times 2)$ unit cell, indicated by a rectangle in Figure 2, by using the DFT calculation. In Figure 2, the formates of configurations A and B are put on the left and right Ti rows in the rectangle, respectively. As mentioned in the previous section, the two O atoms of a formate are located on two neighboring 5-fold coordinated Ti atoms in the bridge configuration A, whereas in the bridge configuration B, one O atom of a formate adsorbs on a 5-fold coordinated Ti atom and the other one adsorbs at an oxygen vacancy site on a bridging O row (denoted by O_B , hereafter). As seen in Figure 2, the bridge configuration A has a symmetric structure, i.e., the two C–O bond lengths are almost equal. On the other hand, the bridge configuration B has an

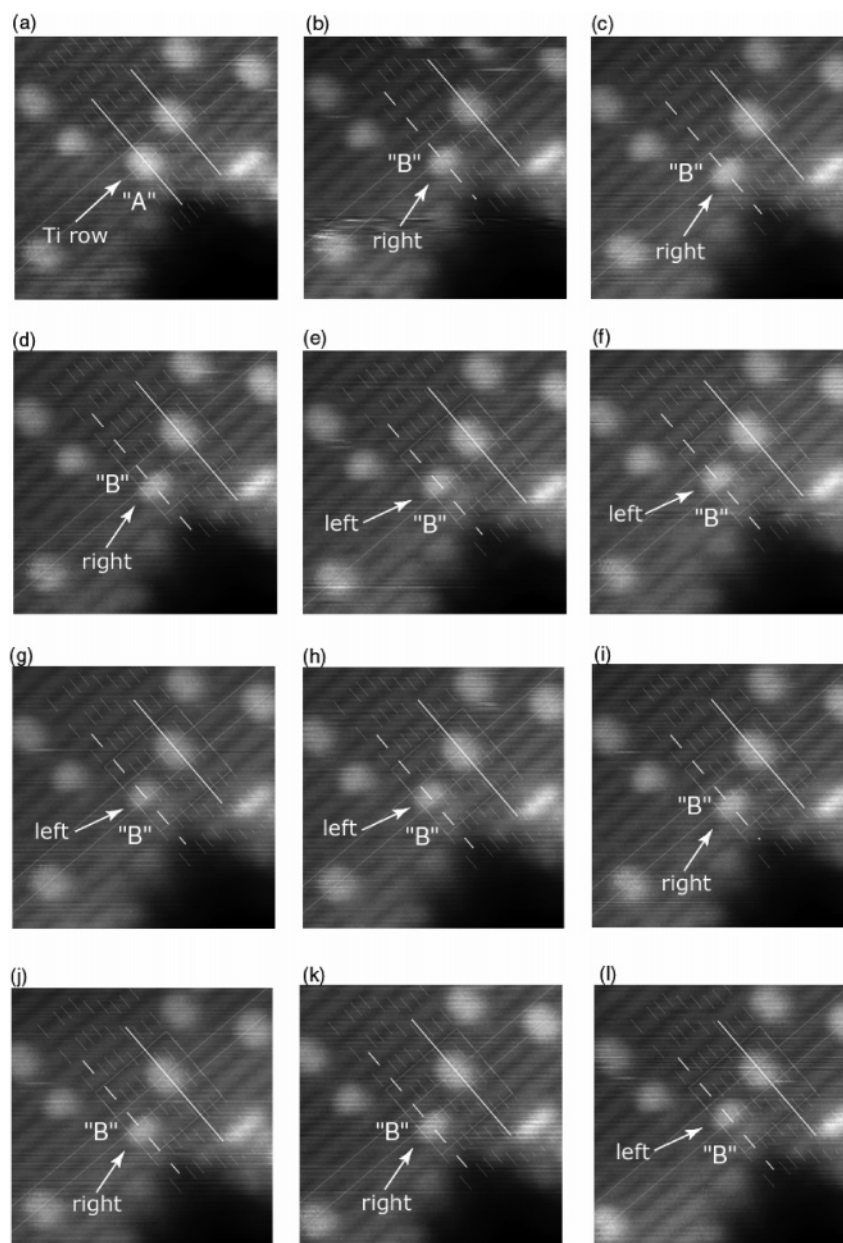


Figure 5. (a–l) Successive STM images of formates on $\text{TiO}_2(110)$ at 350 K (CCT, $7.5 \times 7.5 \text{ nm}^2$, $V_s = 1.2 \text{ V}$, $I_t = 0.1 \text{ nA}$). The time interval of each image was 80 s. $t =$ (a) 0, (b) 80, (c) 160, (d) 240, (e) 320, (f) 400, (g) 480, (h) 560, (i) 640, (j) 720, (k) 800, and (l) 880 s.

asymmetric structure, with a slightly longer C–O bond length (0.130 nm) at the vacancy site than that (0.126 nm) at the 5-fold Ti site. In addition, the heights of the O atoms are different; the O atom at the vacancy site is located about 0.05 nm lower than that at the 5-fold Ti site. Accordingly, the C–H bond of the bridge configuration B is tilted from the surface normal by 11° , and the H height of the bridge configuration B is lower than that of the bridge configuration A by 0.03 nm. The bridge configuration A is the most stable one on the stoichiometric $\text{TiO}_2(110)$ surface, although the bridge configuration B becomes more stable than the bridge configuration A if a vacancy of O_B exists on the surface.

The projected density of states (PDOS) of formates in the two configurations is shown in panels a and b of Figure 3. The density of states projected onto a molecular orbital χ_{MO} is defined by

$$\rho_{\text{MO}}(E) = \sum_{i\mathbf{k}} w_{\mathbf{k}} \langle \chi_{\text{MO}} | \phi_{i\mathbf{k}} \rangle \delta(E - E_{i\mathbf{k}})$$

where $w_{\mathbf{k}}$ is the weight of \mathbf{k} -point sampling, and $\phi_{i\mathbf{k}}$ and $E_{i\mathbf{k}}$ are the eigen wave function and the energy eigenvalue of the i th band of the \mathbf{k} th point, respectively. Panels a and b of Figure 3 show the projected density of state onto the $6a_1$ state and $2b_1$ state for the bridge configurations A and B of formates, respectively. The energy zero is placed at the center of the occupied and empty states of the system. Figure 3c shows the $6a_1$ and $2b_1$ molecular orbitals of the isolated formate anion. The $6a_1$ state is the highest occupied molecular orbital (HOMO) of isolated formate anion, and it has a character of a lone pair state of O 2p. The $2b_1$ state is the LUMO of isolated formate anion, and it has an antibonding character of O–C–O π^* state. In both the bridge configurations A and B, the $6a_1$ state is almost fully occupied and the $2b_1$ state is empty. The greater stability of the bridge configuration B at the vacancy site compared to that of the bridge configuration A can be ascribed to the stabilization of the $6a_1$ state in the bridge configuration B. As can be seen in Figure 3a,b, the $6a_1$ state is located about 0.5 eV lower in the bridge configuration B than that in the bridge

configuration A. The $2b_1$ state of the bridge configuration B is also located about 1.0 eV lower than that of the bridge configuration A. This is presumably due to the longer C–O bond length of the bridge configuration B, because the $2b_1$ state has an antibonding character for the C–O bond, as mentioned above.

Figure 4 shows empty-state STM images of the bridge configurations A and B in a (2×2) unit cell. A formate molecule in the bridge configuration A (right-hand side in Figure 4) exhibits bright protrusion elongated along the $[1\bar{1}0]$ direction, with darker protrusion extended along the $[001]$ direction, indicating the $2b_1$ character. A formate molecule in the bridge configuration B also exhibits the $2b_1$ character, but it is rotated by 90° (left-hand side in Figure 4). The ellipsoidal feature for the bridge formates A and B identifies the two different configurations as perpendicular to each other. At a sample bias of 1.2 V, the bridge configuration B is slightly darker than the bridge configuration A because of the lower position of the molecule. The difference in the relative bright contrasts also identifies the bridge formates A and B in Figure 1a.

3.3. Successive STM Images of a $\text{TiO}_2(110)$ –Formate Surface at 350 K. Successive STM images in the same area at 350 K were observed to explore dynamic processes of formates on a $\text{TiO}_2(110)$ surface on an atomic scale because dynamic transformations of surface formates were considered to be involved in the catalytic decomposition reaction of formic acid.

Figure 5 shows successive STM images recorded at an interval of 80 s. A $\text{TiO}_2(110)$ surface was exposed to 1 L of DCOOD at RT followed by annealing at 350 K for 400 min before the STM imaging. Formate A in image 5a at time = 0 s is seen as an ellipse along the $[1\bar{1}0]$ direction on Ti rows, indicating the bridge configuration A. In image 5b, formate B, indicated by a white arrow, changed into a smaller contrast of an ellipse along the $[001]$ direction. Since the features of the smaller contrast and the ellipse along the $[001]$ direction are characteristic of the bridge configuration B, one can safely conclude that the formate in the configuration A was transformed to the formate in the configuration B at $t = 80$ s. The formate also moved to the right and lower side of the Ti row. White broken lines along the $[1\bar{1}0]$ direction were superimposed on Ti atoms in STM images 5a–l. The interval of the broken lines is 0.296 nm, corresponding to the 1×1 periodicity. The transformation of formate from the A to the B configuration was associated with a shift of the formate along the Ti row by 0.148 nm. This change is schematically illustrated in Figure 6. In image 5b at 80 s, the formate in the bridge configuration B occupies an oxygen vacancy with an oxygen atom of the formate as already discussed. Therefore, an oxygen vacancy must have existed on the formate B site in image 5b.

Another dynamic of formates was also imaged by STM in Figure 5. The location of the bridge formate B remained unchanged until $t = 240$ s. The formate species moved to the left side of the same Ti row in image 5e. The site of the formate B in image 5e corresponds to the mirror site of the formate B in images 5b–d against the Ti row. Thus, another oxygen vacancy should exist on the mirror site of the oxygen vacancy in images 5b–d, although the oxygen vacancies could not be imaged by STM in the presence of adsorbed formates. As a result, hopping of the formate B occurred from an oxygen vacancy site to another oxygen vacancy site across the Ti row. In panels b–l of Figure 5, the hopping between the two bridge formate configurations B was repeated over 880 s at 350 K. The formate B on the left side of the Ti row hops back to the initial formate site on the right-hand side in image 5i after

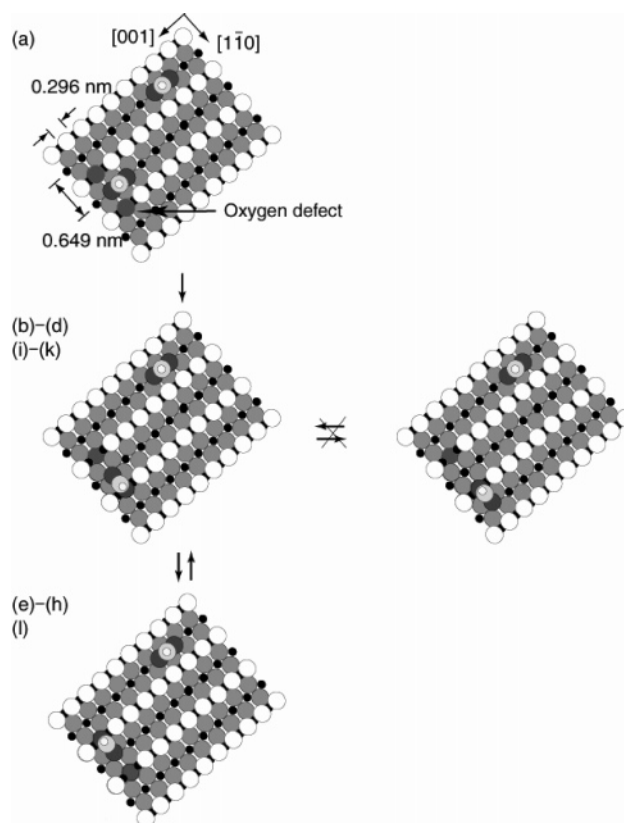


Figure 6. Schematic illustration of the observed dynamics in Figure 5.

640 s, and then to formate B on the left-hand side again in image 5l at 880 s. This repeated dynamic behavior of hopping is illustrated in Figure 6. The frequency (ν) of the hopping event is given by the following equation, assuming an Arrhenius-type surface process

$$\nu = \nu_0 \exp\left(-\frac{E_h}{RT}\right) = \frac{3}{800}$$

where ν_0 , E_h , R , and T represent the frequency factor, activation energy, gas constant, and sample temperature of 350 K, respectively. The observed hopping frequency was three times in 800 s, as shown in Figure 5. Assuming the frequency factor of the hopping event to be a typical value of 10^{13} s^{-1} , the activation energy of the hopping event for the bridge formate B was calculated to be 100 kJ mol^{-1} . During the hopping events, which were observed for seven B species, the formates switched sides of the Ti row without being trapped at the A site, probably because of the inertia effect in an energy profile, with the activation energy for the hopping event from B to A being larger than that from A to B.

The hopping event was observed between the two formate B sites passing across the Ti row, whereas no hopping between two sites across the bridging O row was observed by STM. This may contradict a simple speculation on the Ti–O–formate bond strength. Because the formate oxygen atom is bound to two Ti atoms at the oxygen vacancy, the Ti–O bond may be less easily broken than the Ti–O single bond between the other O atom of the formate and a $\text{Ti}^{(5)}$ atom, favoring the hopping across the bridging O row, unlike the present STM observation (Figure 6). However, one should note that a successive step after the first step of breaking a Ti–O–formate bond is needed for a hopping event: (i) rotation around the other Ti–O–formate bond or (ii) breaking the other Ti–O bond at the oxygen

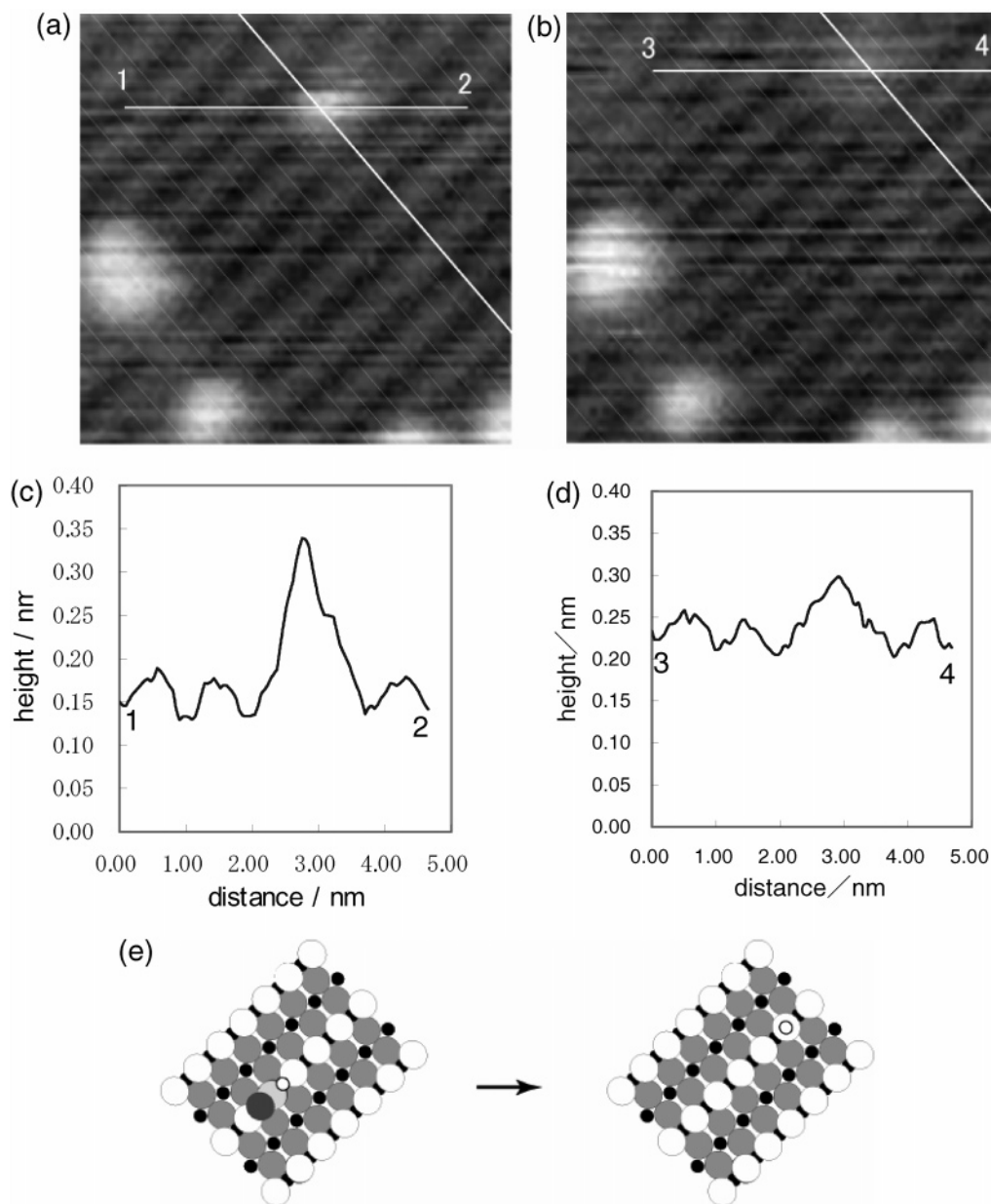


Figure 7. (a,b) Successive STM images ($7.5 \times 7.5 \text{ nm}^2$) taken in the same condition as Figure 5. The H diffused along the oxygen row by a distance of three oxygen atoms from the formate C. (c,d) Line profiles of image (a) (line 1–2) and image (b) (line 3–4), respectively. (e) Schematic illustration of the images (a) and (b).

vacancy site (hopping in the $[1\bar{1}0]$ direction). Since more energy is needed for breaking of the second Ti–O bond, path (ii) is undesirable. Thus, path (i) determines the probability, and the geometry around the formate becomes important. For the hopping across the Ti row observed in Figure 5, the rotation may occur around the $\text{Ti}^{(5)}\text{--O}$ single bond, and the other O of the formate overcomes the Ti row without any significant restriction.

On the other hand, for the hopping across the bridging O row, the rotation should occur around the Ti–O–Ti bonds, which would cause restriction for the rotation, and the other O atom of formate needs to overcome the O row, which is the highest point of the surface. Thus this rotation may be improbable. Hopping across the Ti row via an unstable bidentate formate on a $\text{Ti}^{(5)}$ atom may also be possible. The hopping between the bridge formates across the Ti row is less energetically favorable and more geometrically favorable than that across the O row. The balance between the two factors regulates the hopping possibility.

Finally, we have succeeded in observing the final step of the formate decomposition process by in situ STM at 350 K. Panels a and b of Figure 7 are serial STM images recorded at an interval of 80 s in the same area. The formate species observed in the upper part of Figure 7a is located on the O row, and hence it is assigned as monodentate formate C, as already discussed. The monodentate formate changed to a rather faint protrusion, and moved upward along the O row by a three lattice unit distance (0.89 nm). The change in the contrast and position may reflect the occurrence of a surface reaction from the monodentate formate to the other species. To study this surface event in more detail, we took the line profiles along the line 1–2 in Figure 7a and the line 3–4 in Figure 7b. The obtained line profiles are shown in Figure 7c,d. The monodentate formate C was imaged as a protrusion of 0.18 nm height, measured from the Ti row. This high protrusion changed to a smaller one of 0.05 nm height protrusion in 80 s at 350 K. Compared with STM images of hydrogen atoms stabilized on the bridging O atoms in the previous study,⁶¹ the protrusion is assigned to a surface OH

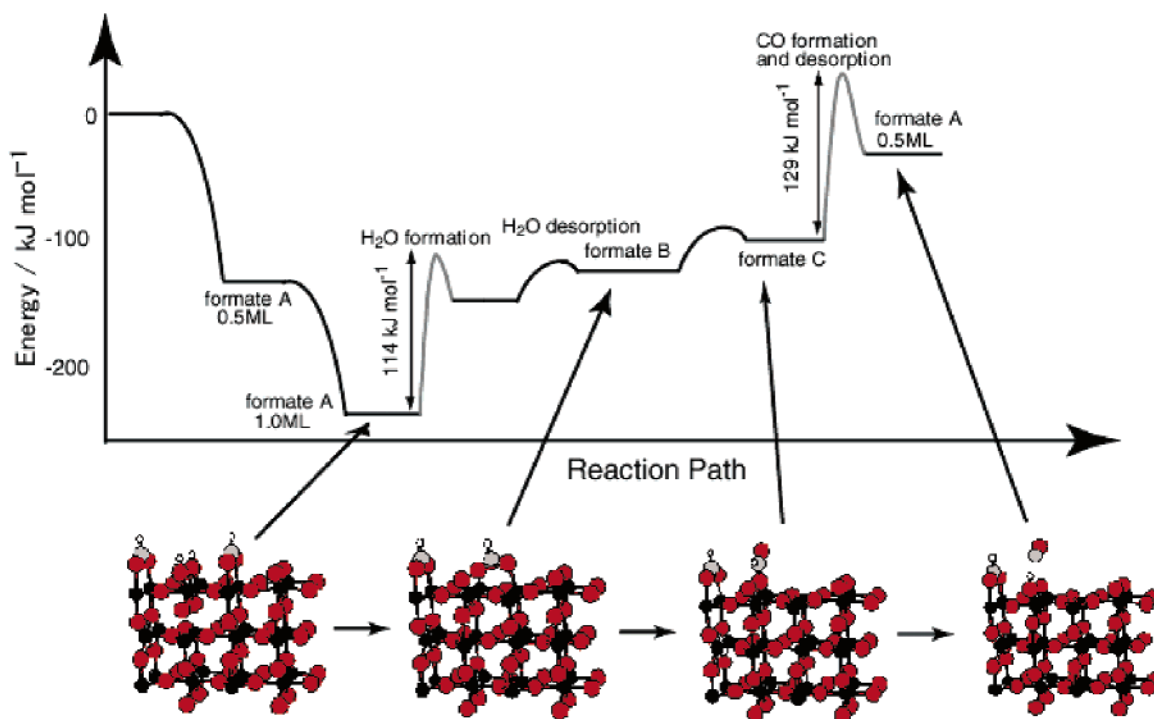
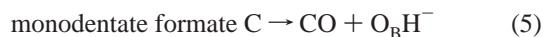
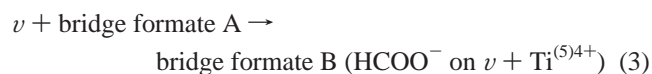
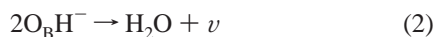
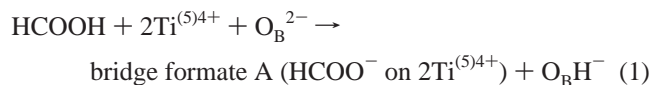


Figure 8. Energy diagram for the dehydration process of HCOOH on the $\text{TiO}_2(110)$ surface by DFT calculation. The energy of 0.5 ML of formate on the left is the energy of one adsorbed formate A and one gas-phase formic acid molecule, while the energy of 0.5 mL of formate on the right is the energy of one adsorbed formate A, one gas-phase water molecule, and one gas-phase CO molecule.

group on the bridging oxygen row. The transformation of the adsorbed monodentate formate species to the hydroxyl is illustrated in Figure 7e. Our previous DFT calculations revealed that the hydrogen atom of the monodentate formate adsorbed on an oxygen vacancy interacted with an adjacent bridging oxygen atom (O_B) at the transition state of the decomposition reaction, and the C–H bond of the formate is broken, resulting in OH formation and evolving CO in the gas phase.¹¹ The OH species should be observed at the site adjacent to the monodentate formate. However, the OH species was actually imaged on the bridging O_B atom that was more than two lattice units away from the O_B atom adjacent to the original monodentate formate site.

The transformations of formates from the configuration A to the configurations B and C can be explained by the calculated energy diagram for the dehydration process of formic acid on $\text{TiO}_2(110)$, which is shown in Figure 8. Formic acid dissociatively adsorbs to form a formate (HCOO^-) on the two 5-fold coordinated $\text{Ti}^{(5)}_5$ atoms in the bridge configuration A, with the O–C–O plane parallel to the [001] direction, and with the formic acid proton (H^+) and a bridging oxygen anion (O_B^{2-}) forming a hydroxyl ($\text{O}_\text{B}\text{H}^-$) (eq 1). From two $\text{O}_\text{B}\text{H}^-$ molecules, one H_2O molecule forms by dehydration, leaving an oxygen vacancy (ν) (eq 2).



Thus, for an overall reaction



The energy diagram for this process is shown in Figure 8.¹¹ The activation barrier was calculated to be 114 kJ mol^{-1} ,¹¹ and the desorption temperature of H_2O from a $\text{TiO}_2(110)$ surface exposed to formic acid was reported to be 370 K.²⁶ At the present STM imaging temperature of 350 K, the H_2O formation accompanied by the formation of an oxygen vacancy readily occurs. It is to be noted that oxygen vacancies can be produced in situ under the catalytic dehydration reaction of formic acid on $\text{TiO}_2(110)$, even if there were no oxygen vacancy on the intrinsic $\text{TiO}_2(110)$ surface. The bridge formate A moves to an oxygen vacancy to be stabilized as a bridge formate configuration B with the O–C–O plane parallel to the $[1\bar{1}0]$ direction (eq 3). Alternatively, the formate B may also be formed by direct collision of gas-phase formic acid with the oxygen vacancy site. The bridge formate B is transformed to monodentate formate C on the oxygen vacancy site (eq 4), and then the monodentate formate decomposes to CO and $\text{O}_\text{B}\text{H}^-$, as illustrated in Figure 8. The monodentate formate C is 25 kJ mol^{-1} less stable than the bridge formate B. The activation barrier of the monodentate formate decomposition was calculated to be 129 kJ mol^{-1} , which is similar to the observed activation energy of 120 kJ mol^{-1} ²⁶ (eq 5).

Conclusion

We have performed in situ STM observations of the behavior and decomposition process of formic acid on a $\text{TiO}_2(110)$ surface at 350 K. Three different formate intermediates were identified by their shapes and locations in the STM images. The configurations of the formate species were also determined by the first-principle DFT calculation. We have also visualized dynamic transformations among formates A and B and the hopping processes of these formate species by successive STM

observations at 350 K. The observed aspects are consistent with the energy diagram obtained by the theoretical calculations. The whole reaction paths of formic acid dehydration on TiO₂(110) were elucidated to proceed at oxygen vacancies.

Acknowledgment. This study was supported by a grant-in-aid for The 21st Century COE Program for Frontiers in Fundamental Chemistry from the Ministry of Education, Culture, Sports, Science and Technology. Y.M. is supported by Japan Science and Technology Corporation through ACT-JST. The numerical calculations were carried out at the computer centers of Tsukuba Advanced Computing Center (TACC), Institute for Solid State Physics, the University of Tokyo, Kyoto University, Kyushu University, and Nagoya University.

References and Notes

- (1) Henrich, V. E.; Cox, P. A. *The Surface Science of Metal Oxides*; Cambridge University Press: Cambridge, U.K., 1994.
- (2) Henry, C. R. *Surf. Sci. Rep.* **1998**, *31*, 235.
- (3) Valden, M.; Lai, X.; Goodman, D. W. *Science* **1998**, *281*, 1647.
- (4) Sanches, A.; Abbet, S.; Heiz, U.; Schneider, W.-D.; Hakkinen, H.; Barnett, R. N.; Landman, U. *J. Phys. Chem. A* **1999**, *103*, 9573.
- (5) Campbell, C. T.; Parker, S. C.; Starr, D. E. *Science* **2002**, *298*, 811.
- (6) Grätzel, M. *Nature* **2001**, *414*, 338.
- (7) Serpone, N.; Pelizzetti, E., Eds. *Photocatalysis: Fundamentals and Applications*; Wiley: New York, 1989.
- (8) Linsebigler, A.; Lu, G.; Yates, J. T. *Chem. Rev.* **1995**, *95*, 735.
- (9) Kasemo, B.; Gold, J. *Adv. Dent. Res.* **1999**, *13*, 8.
- (10) Diebold, U. *Surf. Sci. Rep.* **2002**, *293*, 1.
- (11) Iwasawa, Y.; Onishi, H.; Fukui, K.; Suzuki, S.; Sasaki, T. *Faraday Discuss.* **1999**, *114*, 259.
- (12) Fukui, K.; Takakusagi, S.; Tero, R.; Aizawa, M.; Namai, Y.; Iwasawa, Y. *J. Phys. Chem. Chem. Phys.* **2003**, *5*, 5349.
- (13) Namai, Y.; Fukui, K.; Iwasawa, Y. *Catal. Today* **2003**, *85*, 79.
- (14) Namai, Y.; Fukui, K.; Iwasawa, Y. *Nanotechnology* **2004**, *15*, S49.
- (15) Over, H.; Kim, Y. B.; Seitonen, A. P.; Wendt, S.; Lundgren, E.; Schmid, M.; Varga, P.; Morgante, A.; Ertl, G. *Science* **2000**, *287*, 1474.
- (16) Schaub, R.; Wahlström, E.; Rønnau, A.; Lægsgaard, E.; Stensgaard, I.; Besenbacher, F. *Science* **2003**, *299*, 377.
- (17) Onishi, H.; Iwasawa, Y. *Surf. Sci. Lett.* **1994**, *313*, L783.
- (18) Onishi, H.; Fukui, K.; Iwasawa, Y. *Bull. Chem. Soc. Jpn.* **1995**, *68*, 2447.
- (19) Vohs, J. M.; Barteau, M. A. *Surf. Sci.* **1986**, *176*, 91.
- (20) Henderson, M. A. *J. Phys. Chem.* **1995**, *99*, 15253.
- (21) Idriss, H.; Lusvardi, V. S.; Barteau, M. A. *Surf. Sci.* **1996**, *348*, 39.
- (22) Nakatsuji, H.; Yoshimoto, M.; Umemura, Y.; Takagi, S.; Hada, M. *J. Phys. Chem.* **1996**, *100*, 694.
- (23) Bandara, A.; Kubota, J.; Onda, K.; Wada, A.; Kano, S. S.; Domen, K.; Hirose, C. *J. Phys. Chem. B* **1998**, *102*, 5951.
- (24) Vittadini, A.; Selloni, A.; Rotzinger, F. P.; Graetzel, M. *J. Phys. Chem. B* **2000**, *104*, 1300.
- (25) Onishi, H.; Aruga, T.; Egawa, C.; Iwasawa, Y. *Surf. Sci.* **1988**, *193*, 33.
- (26) Onishi, H.; Aruga, T.; Iwasawa, Y. *J. Am. Chem. Soc.* **1993**, *115*, 10460.
- (27) Onishi, H.; Iwasawa, Y. *Chem. Phys. Lett.* **1994**, *226*, 111.
- (28) Onishi, H.; Iwasawa, Y. *Jpn. J. Appl. Phys.* **1994**, *33*, L1338.
- (29) Onishi, H.; Aruga, T.; Iwasawa, Y. *J. Catal.* **1994**, *146*, 557.
- (30) Onishi, H.; Iwasawa, Y. *Langmuir* **1994**, *10*, 4414.
- (31) Onishi, H.; Fukui, K.; Iwasawa, Y. *Colloids Surf., A* **1996**, *109*, 335.
- (32) Onishi, H.; Iwasawa, Y. *Surf. Sci.* **1996**, *357/358*, 773.
- (33) Iwasawa, Y. *Catal. Surv. Jpn.* **1997**, *1*, 3.
- (34) Onishi, H.; Iwasawa, Y. In *Interfacial Science: A Chemistry for the 21st Century Monograph*; Roberts, M. W., Ed.; Blackwell Science: Oxford, U.K., 1997; pp 57–75.
- (35) Henderson, M. A. *J. Phys. Chem. B* **1997**, *101*, 221.
- (36) Fukui, K.; Onishi, H.; Iwasawa, Y. *Chem. Phys. Lett.* **1997**, *280*, 296.
- (37) Wang, L. Q.; Ferris, K. F.; Shultz, A. N.; Baer, D. R.; Engelhard, M. H. *Surf. Sci.* **1997**, *380*, 352.
- (38) Chambers, S. A.; Thevuthasan, S.; Kim, Y. J.; Herman, G. S.; Wang, Z.; Tober, E.; Ynzunza, R.; Morais, J.; Peden, C. H. F.; Ferris, K.; Fadley, C. S. *Chem. Phys. Lett.* **1997**, *267*, 51.
- (39) Bates, S. P.; Kresse, G.; Gillan, M. J. *Surf. Sci.* **1998**, *409*, 336.
- (40) Hayden, B. E.; King, A.; Newton, M. A. *J. Phys. Chem. B* **1999**, *103*, 203.
- (41) Fukui, K.; Onishi, H.; Iwasawa, Y. *Appl. Surf. Sci.* **1999**, *140*, 259.
- (42) Kaeckell, P.; Terakura, K. *Surf. Sci.* **2000**, *461*, 191.
- (43) Iwasawa, Y.; Onishi, H.; Fukui, K. *Top. Catal.* **2001**, *14*, 163.
- (44) Bowker, M.; Stone, P.; Bennett, R.; Perkins, N. *Surf. Sci.* **2002**, *511*, 435.
- (45) Wang, Q.; Biener, J.; Guo, X. C.; Farfan-Arribas, E.; Madix, R. J. *J. Chem. Phys. B* **2003**, *107*, 11709.
- (46) Chang, Z.; Thornton, G. *Surf. Sci.* **2000**, *462*, 68.
- (47) Gutiérrez-Sosa, A.; Martínez-Escobedo, P.; Raza, H.; Lindsay, R.; Wincott, P. L.; Thornton, G. *Surf. Sci.* **2001**, *471*, 163.
- (48) Morikawa, Y.; Takahashi, I.; Aizawa, M.; Namai, Y.; Sasaki, T.; Iwasawa, Y. *J. Phys. Chem. B* **2004**, *108*, 14446.
- (49) Yamaguchi, Y.; Onishi, H.; Iwasawa, Y. *J. Chem. Soc., Faraday Trans.* **1995**, *91*, 1663.
- (50) Morikawa, Y. *Phys. Rev. B* **2001**, *63*, 033405.
- (51) Morikawa, Y.; Iwata, K.; Terakura, K. *Appl. Surf. Sci.* **2001**, *169*, 11.
- (52) Morikawa, Y.; Liew, C. C.; Nozoye, H. *Surf. Sci.* **2002**, *514*, 389.
- (53) Okamoto, Y.; Sugino, O.; Mochizuki, Y.; Ikeshoji, T.; Morikawa, Y. *Chem. Phys. Lett.* **2003**, *377*, 236.
- (54) Okazaki, K.; Morikawa, Y.; Tanaka, S.; Tanaka, K.; Kohyama, M. *Phys. Rev. B* **2004**, *69*, 235404.
- (55) Hohenberg, P.; Kohn, W. *Phys. Rev.* **1964**, *136*, B184.
- (56) Kohn, W.; Sham, L. J. *Phys. Rev.* **1965**, *140*, A1133.
- (57) Perdew, J. P.; Burke, K.; Ernzerhof, M. *Phys. Rev. Lett.* **1996**, *77*, 3865.
- (58) Vanderbilt, D. *Phys. Rev. B* **1991**, *41*, 7892.
- (59) Troullier, N.; Martins, L. J. *Phys. Rev. B* **1991**, *43*, 1993.
- (60) Tersoff, J.; Hamann, D. R. *Phys. Rev. B* **1985**, *31*, 805.
- (61) Suzuki, S.; Fukui, K.; Onishi, H.; Iwasawa, Y. *Phys. Rev. Lett.* **2000**, *84*, 2154.